energy&fuels

pubs.acs.org/EF

Communication

Construction of an Electron Bridge in Polyoxometalates/Graphene Oxide Ultrathin Nanosheets To Boost the Lithium Storage Performance

Jia-Nan Chang,[†] Mi Zhang,[†] Guang-Kuo Gao,[†] Meng Lu, Yi-Rong Wang, Cheng Jiang, Shun-Li Li, Yifa Chen,* and Ya-Qian Lan*

Cite This: *Energy Fuels* 2020, 34, 16968−16977

Read Online

ACCESS | Metrics & More | Article Recommendations | Supporting Information

ABSTRACT: Polyoxometalates (POMs), possessing multiple-electron redox ability, controllable size, and precise structure, hold much promise to be applied as anode materials in lithium-ion batteries (LIBs). However, the applications of them have been largely limited by the low conductivity and dissolution in an electrolyte. Herein, we report a series of covalently connected $MnMo_6$−$2NH_2$−GO ultrathin nanosheets (as thin as ∼1.1 nm), in which $MnMo_6$−$2NH_2$ as the electron sponge is covalently linked to graphene oxide and the covalent bond as the electron bridge is highly adventurous for battery applications. Specifically, $MnMo_6$−$2NH_2$−GO-2 presents a reversible capacity of 1143 mAh g^{-1} (0.1 A g^{-1}) after 100 cycles, and the capacity retention is nearly 100% at 1000 mA g^{-1} over 500 cycles. In addition, it also shows excellent rate capability (301 mAh g^{-1} in 5 A g^{-1}). This work paves a new way in designing POM-based novel electrode materials for high-performance LIBs.

1. INTRODUCTION

The yearly increasing pollution problem caused by fuel burning has transferred the attention of scientists from the fuel-energy-related area to green power supply techniques.[1−3] Power supply techniques, such as lithium-ion batteries (LIBs), have envisioned prosperous development during the past few decades, owing to the huge energy demand for application scenarios, such as portable devices (e.g., cellphones or laptops), vehicles, utility industry, etc.[4−7] The production of LIBs around the world has reached 316 GWh in 2019 and is predicted to reach more than 1200 GWh in 2025.[8] The vital roles of LIBs in the power-supply field are ascribed to their higher energy density compared to other rechargeable battery systems, enabled by the design and development of high-performance electrode matrials.[7,9−12] However, the commonly applied graphite-based anodes show relatively low practical capacity and poor rate capability, which still hampers their further development to meet the booming requirements of energy supply.[13−15] Besides, the safety issues caused by the problems, such as Li dendrite, have largely obstructed the development of broader application areas, especially for the more and more strict demand for powerful devices coupling with the novel techniques altered from day to day.[16−18] It has become an important target all around the world to explore novel, safe, and low-cost LIB anode materials with high capacity and excellent rate or cycling performance.

Polyoxometalates (POMs) are a class of anionic polynuclear metal oxides based on high-valence transition metals, such as V, Mo, and W, possessing advantages, such as redox properties, nanosize, tunable topology, and O-enriched surfaces.[19−22] They have shown much promise in diverse applications, such as energy storage, catalysis, sensing, proton conductivity, etc.[23−26] As one of the most promising candidates, POMs with multiple-electron redox characteristics and high chemical and thermodynamic stability are suitable for the applications of LIBs,[27−29] especially for the redox properties of POMs that can reversibly withdraw and donate electrons (called an "electron sponge" or "electron-rich aggregates") during the electrochemical process, which is also much more beneficial for the potential applications in LIBs.[30−34] However, there are still two inevitable problems that obstruct the applications of POMs in LIBs: the low conductivity and potential dissolution in an electrolyte, which have largely affected the cycling stability of POMs and limited their further applications in LIBs. To overcome these shortcomings, a series of strategies have been investigated to improve the upper limit of POMs for the potential applications of LIBs and can be mainly classified into two categories: the physical mixing POMs with conducting materials or the direct growth of POMs onto the surface of conductive materials. For the physical mixing method, POMs, such as $MnMo_6$ or $Na_3[AlMo_6O_{24}H_6]$, have been physically mixed with conductive materials, such as carbon substrates [e.g., Ketjen Black, carbon nanotubes (CNTs), etc.] to investigate their LIB performance.[35,36] However, the non-uniformly distributed morphology or separated phase of them are limited in the interface contact and ion/electron transfer, which has resulted in insufficient activity of the mixed materials. For the direct growth methods, various POMs or

Received: October 19, 2020
Revised: October 29, 2020
Published: November 9, 2020

https://dx.doi.org/10.1021/acs.energyfuels.0c03482
Energy Fuels 2020, 34, 16968−16977

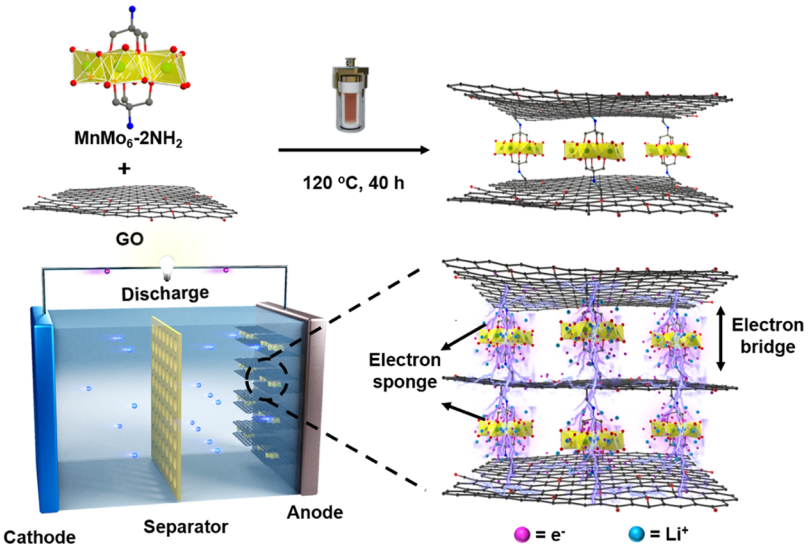

Figure 1. Schematic illustration of the formation of $MnMo_6$−$2NH_2$−GO-*x*.

POM-based catalysts have grown onto the surface of conductive materials, such as CNTs or graphene oxide (GO).[37,38] However, most of the interactions generated during this process are weak interactions, such as hydrogen bonds or intermolecular forces, and the uniform dispersion of POMs is still challenging. Therefore, it might be more desirable to produce POM-based hybrid materials with stronger interactions, such as a covalent band, to explore their potential applications in LIBs, in which the covalent band would largely improve the dispersion, stability, or transmission of POMs and inhibit the dissolution of POMs in electrolytes.

As a proof of concept, we decide to assemble $MnMo_6$−$2NH_2$ and GO to construct covalently connected hybrid materials (Figure S1 of the Supporting Information). The corresponding considerations are listed as follows: (1) $MnMo_6$−$2NH_2$, including six Mo^{6+}, is easily transferred into the mixed valence state of Mo^{4+} and Mo^{6+} when triggered by the redox reaction or bias stimulus, serving as an "electron sponge" that can easily donate and withdraw electrons;[39,40] (2) GO, where the inherent epoxy functional groups can interact with the amino groups in $MnMo_6$−$2NH_2$ to generate covalent bonds, has proven to be a desirable conductive platform;[41−44] (3) the connection between $MnMo_6$−$2NH_2$ and GO will presumably create an electron transportation pathway (also called "electron bridge") under the motivation of an electric field to facilitate the multiple electron-donating/withdrawing process; and (4) the covalent bond generated between $MnMo_6$−$2NH_2$ and GO can guarantee the strong interaction to facilitate the uniform dispersion of $MnMo_6$−$2NH_2$ and inhibit the dissolution of $MnMo_6$−$2NH_2$ in electrolytes, thus improving the battery properties. From the above, we deduce that the hybrid materials that covalently connect $MnMo_6$−$2NH_2$ and GO will probably be the promising candidates in LIBs, while the assembly of this type of material has been rarely reported.

Herein, we have facilely synthesized a series of $MnMo_6$−$2NH_2$−GO hybrid materials through a one-pot hydrothermal method (Figure 1). The synergistic combination of $MnMo_6$−$2NH_2$ and GO in these hybrid materials can indeed serve the role of gathering a redox component and conductive substrate in a system to overcome the problems of solubility and poor conductivity of POMs. $MnMo_6$−$2NH_2$ as the electron sponges can be covalently connected with GO, and the connection would serve as an electron bridge, highly advantageous for the redox process, ion/electron transfer, dispersion, or stability of POMs. As expected, these hybrid materials present high performance in LIBs. The best of them, $MnMo_6$−$2NH_2$−GO-2, exhibits excellent cycling performance and achieves a high capacity as a LIB anode, which can deliver a high discharge capacity of 1143 mAh g^{-1} at 100 mA g^{-1} after 100 cycles as well as impressive rate capability (301 mAh g^{-1} in 5 A g^{-1}). The high performance of $MnMo_6$−$2NH_2$−GO hybrid materials might be ascribed to the covalent bonds generated between POMs and GO as supported by sufficient contrast experiments and characterizations. This work paves a new avenue in designing novel electrode materials based on POMs and conductive materials and might advance the applications of POMs in LIBs.

2. EXPERIMENTAL SECTION

2.1. Material Preparation. *2.1.1. Synthesis of $[N(C_4H_9)_4]_4[\alpha$-$Mo_8O_{26}]$.* $[N(C_4H_9)_4]_4[\alpha$-$Mo_8O_{26}]$ was synthesized according to the reported literature.[14] $C_{16}H_{36}BrN$ (3.34 g) was dissolved in distilled water (10 mL). Then, Na_2MoO_4 (5 g) was dissolved in mixed solution of distilled water (12 mL) and HCl (5.17 mL, 6 M) and stirred for 2 min. Then, $C_{16}H_{36}BrN$ solution was added to Na_2MoO_4 solution under stirring. The product was filtered and washed thoroughly with water, ethanol, acetone, and ether. A kind of white powder was obtained after drying at 80 °C under vacuum for 12 h.

2.1.2. Synthesis of $[N(C_4H_9)_4]_3[MnMo_6O_{18}\{(OCH_2)_3CNH_2\}_2]$ ($MnMo_6$−$2NH_2$). $[N(C_4H_9)_4]_4[\alpha$-$Mo_8O_{26}]$ (8.00 g, 3.7 mmol), $Mn(CH_3COO)_3{\cdot}2H_2O$ (1.49 g, 5.6 mmol), and $C_4H_{11}NO_3$ (1.56 g, 12.8 mmol) were mixed and dissolved in acetonitrile (150 mL) in a 250 mL round-bottom flask. After refluxing at 80 °C for 16 h in an oil bath and cooling to room temperature, the obtained orange solution is then filtered to remove the unreacted residues. Then, the filtrate was exposed to ether vapor by a solvent diffusion method, and the resulted white precipitate was filtered out after 2 h. After that, the filtered orange solution was exposed to the ether vapor again and orange crystals were obtained after a few days. The final product was collected after filtration, washing with acetonitrile and drying at 80 °C under vacuum for 12 h.

2.1.3. Synthesis of $(NH_4)_4[MnMo_6O_{24}H_6]{\cdot}5H_2O$ ($MnMo_6$). $MnSO_4$ (0.453 g, 3 mmol) was dissolved in distilled water (20 mL), and then the above solution was added to 80 mL of water solution containing $(NH_4)_6Mo_7O_{24}{\cdot}4H_2O$ (5 g, 4.2 mmol) under stirring. After that, 300

https://dx.doi.org/10.1021/acs.energyfuels.0c03482
Energy Fuels 2020, 34, 16968−16977

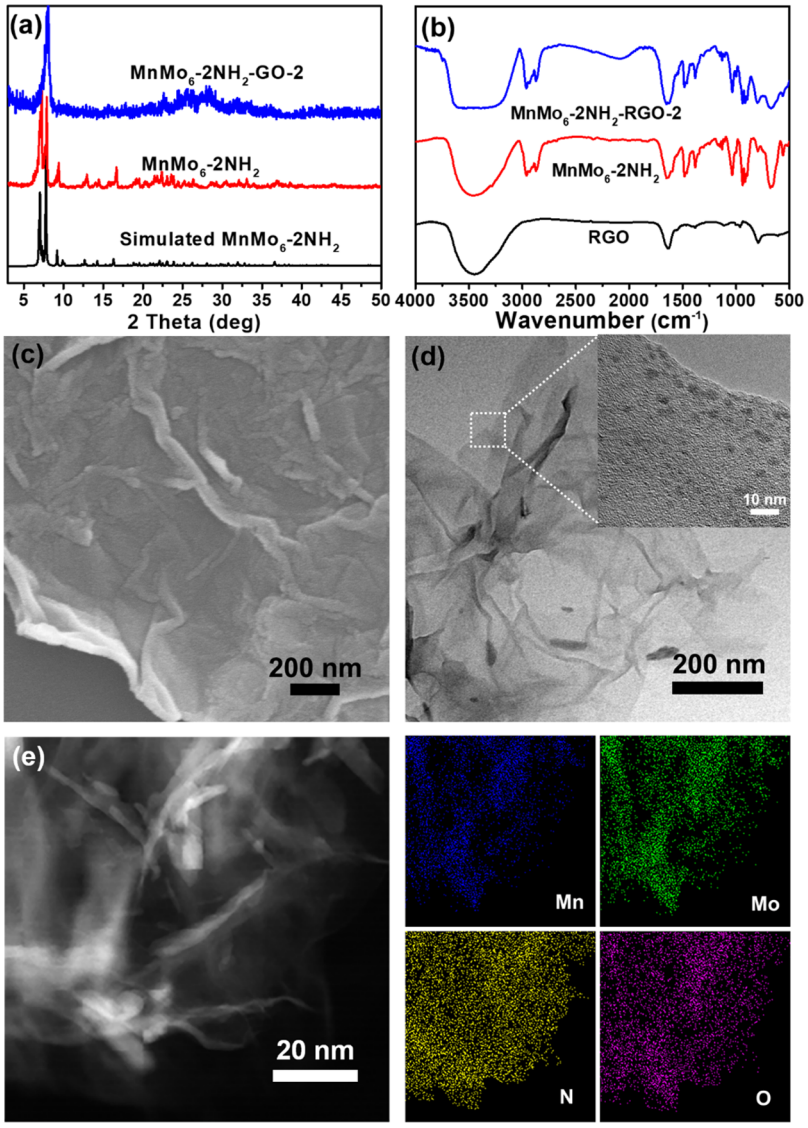

Figure 2. Characterization of $MnMo_6$−$2NH_2$−GO-2: (a) PXRD patterns of $MnMo_6$−$2NH_2$ and $MnMo_6$−$2NH_2$−GO-2, (b) FTIR spectra of $MnMo_6$−$2NH_2$−GO-2, $MnMo_6$−$2NH_2$, and $MnMo_6$/GO, (c) SEM image of $MnMo_6$−$2NH_2$−GO-2, (d) TEM image of $MnMo_6$−$2NH_2$−GO-2 (inset is the square in panel d), and (e) EDS elemental mapping images of Mn, Mo, N, and O.

mL of acetone was slowly added to the solution, and brownish yellow power was obtained by filtration.

2.1.4. Synthesis of $MnMo_6$−$2NH_2$−GO-x (x = 1−5). GO was prepared according to reported methods with slight modification.[55] The $MnMo_6$−$2NH_2$−GO-x (x = 1−5) were synthesized through a facile hydrothermal method. Taking $MnMo_6$−$2NH_2$−GO-2 for instance, first, GO (0.01 g, 0.83 mmol) was dispersed in distilled water (10 mL) with ultrasound for 30 min to produce a suspension with a concentration of 1 mg mL^{-1}. Then, $MnMo_6$−$2NH_2$ (0.153 g, 0.08 mmol) was added to the suspension, followed by stirring for 30 min. The suspension was then transferred into a 20 mL autoclave and heated at 120 °C for 40 h. After cooling to room temperature, the product is filtered and washed with H_2O and ethanol each 3 times. The product was then dried at 100 °C under vacuum for 24 h. As a comparison, $MnMo_6$−$2NH_2$−GO-1 and $MnMo_6$−$2NH_2$−GO-3 were synthesized through the same procedures, except that 0.04 and 0.16 mmol of $MnMo_6$−$2NH_2$ were used to replace 0.08 mmol of $MnMo_6$−$2NH_2$. We have also synthesized $MnMo_6$−$2NH_2$−GO-4 and $MnMo_6$−$2NH_2$−GO-5 with different GO contents, applying a similar method, except that the GO concentrations were changed to 0.5 and 2 mg mL^{-1}.

2.2. Material Characterization. Fourier transform infrared spectroscopy (FTIR) was collected by the KBr method on the spectrometer of NEXUS 670. Powder X-ray diffraction (PXRD) patterns were recorded on a D/max 2500VL/PC diffractometer (Japan) equipped with a graphite monochromatized Cu Kα radiation source (λ = 1.54060 Å). The corresponding working voltage and current are 40 kV and 100 mA, respectively. JEOL-2100F and JEOL-JSM-6700m transmission electron microscopes were used to characterize the morphology of transmission electron microscopy (TEM) and high-resolution transmission electron microscopy (HR-TEM). The accelerating voltage was 200 and 300 kV, respectively. Scanning electron microscopy (SEM) tests were recorded on JEOL-JSM-7600F, and the accelerating voltage was 0.1−30 kV. Nitrogen adsorption−desorption isotherms were recorded at 77 K using a Quantachrome instrument (Quantachrome Instruments Autosorb IQ2).

2.3. Electrochemical Characterization. The samples were treated to remove water before they were used as battery electrodes. The working electrodes were prepared by mixing 70 wt % active material, 20 wt % acetylene black (Super-P), and 10 wt % polyvinylidene fluoride (PVDF) in *N*-methyl-2-pyrrolidinone (NMP). The mixture was ground into a kind of uniform slurry and

https://dx.doi.org/10.1021/acs.energyfuels.0c03482
Energy Fuels 2020, 34, 16968−16977

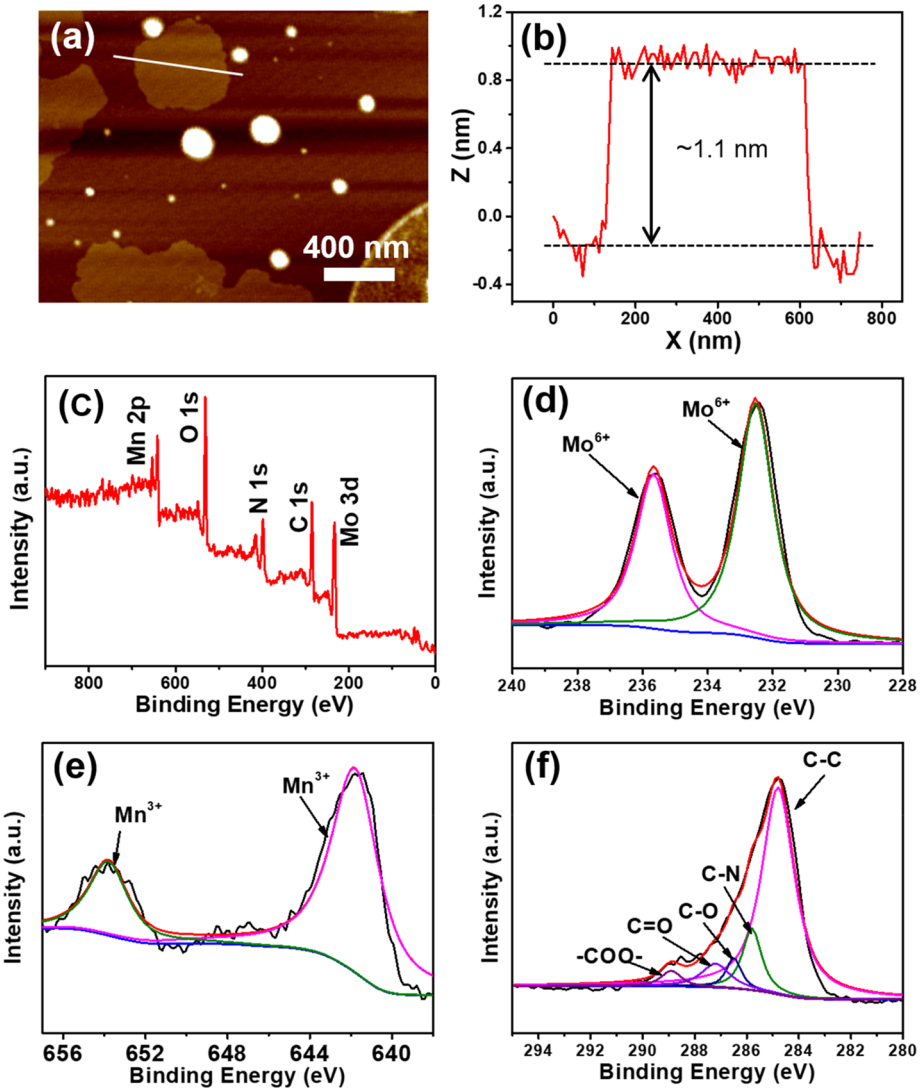

Figure 3. AFM and XPS spectra of $MnMo_6$−$2NH_2$−GO-2: (a) AFM topographical image, (b) height profile of the presented line in panel a, (c) XPS spectra of $MnMo_6$−$2NH_2$−GO-2, (d) Mo 3d, (e) Mn 2p, and (f) C 1s.

drop-casted on the Cu foils with the same thickness. After drying at 90 °C for 6 h to remove NMP, the coating electrode was obtained. Then, the coating electrode were cut into a round pellet with a diameter of 14 mm by a stamping die and then dried at 90 °C under vacuum for 24 h. After cooling to room temperature, the electrode was weighed, and the loading of the active substance on the electrode was about 1 mg. The button half battery used a CR2032 shell and was assembled in a glovebox filled with high-purity argon, where water and oxygen concentrations were strictly limited to less than 1 ppm. In the battery, lithium metal was applied as the counter electrode and Celgard 2400 membrane was applied as the diaphragm to separate the positive and negative electrodes. The electrolyte was a mixture of $C_3H_4O_3$ and $C_3H_6O_3$ (volume ratio of 1:1) containing 1 M $LiPF_6$.

Electrochemical impedance spectroscopy (EIS) measurements and cyclic voltammetry (CV) were conducted on a CHI 660e (Shanghai, China) electrochemical workstation. CV curves were tested from 0.02 to 10 mV s^{-1}, and voltage was from 0.01 to 3 V versus Li/Li^+. The EIS frequency was selected ranging from 100 kHz to 0.01 Hz. The battery-measuring system (CT2001A, Landt, China) was applied to complete the constant current charge and discharge tests of electrode materials at room temperature. The current density was selected from 50 to 3000 mA g^{-1}, and the voltage range was from 0.01 to 3 V versus Li/Li^+. The specific capacity was calculated on the basis of the total mass analysis of the active substance.

3. RESULTS AND DISCUSSION

The preparation procedures of $MnMo_6$−$2NH_2$−GO-x (x = 1−5, which stands for the various ratios of $MnMo_6$−$2NH_2$ and GO) are listed as follows: When $MnMo_6$−$2NH_2$−GO-2 is taken as an example, a mixture of GO and $MnMo_6$−$2NH_2$ was treated at 120 °C for 40 h, followed by washing with H_2O and ethanol each 3 times. The obtained product was then dried under vacuum at 100 °C for 24 h. Upon tuning the ratios of precursors added, hybrid materials with different $MnMo_6$−$2NH_2$ and GO contents were synthesized under similar hydrothermal conditions. The PXRD tests were used to characterize the crystal phases (Figure 2a). $MnMo_6$−$2NH_2$−GO-2 exhibits remaining crystalline integrity of $MnMo_6$−$2NH_2$ when compared to that of $MnMo_6$−$2NH_2$ and GO (Figure 2a). Similarly, $MnMo_6$−$2NH_2$−GO-x (x = 1, 3, 4, and 5) show approximate peak patterns, in good agreement with that of $MnMo_6$−$2NH_2$−GO-2, confirming the high phase purity and good crystallinity (Figure S2 of the Supporting Information). Furthermore, the SEM and TEM tests have been conducted to reveal the morphology of these samples. $MnMo_6$−$2NH_2$−GO-2 displays large-scale and thin nanosheet morphology, consistent with the morphology of GO (Figure 2c

https://dx.doi.org/10.1021/acs.energyfuels.0c03482
Energy Fuels 2020, 34, 16968−16977

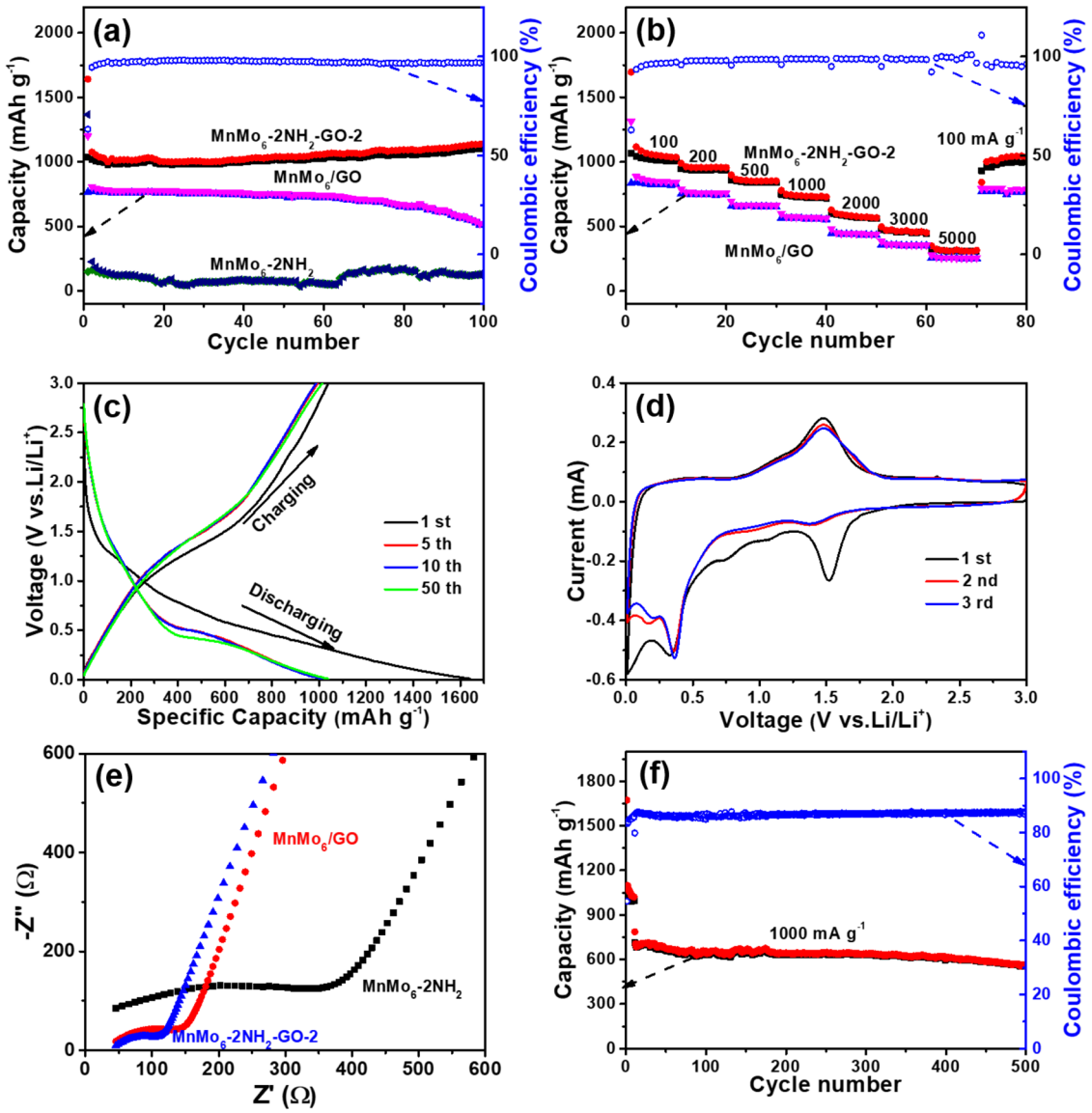

Figure 4. Electrochemical performance of the $MnMo_6$−$2NH_2$−GO-2 hybrid material and other comparative samples: (a) cycling performance at a current density of 100 mA g^{-1}, (b) cycling performance at various current densities, (c) charge/discharge profiles of $MnMo_6$−$2NH_2$−GO-2 for different cycles constantly at 50 mA g^{-1}, (d) CV profiles of $MnMo_6$−$2NH_2$−GO-2 at a scan rate of 0.2 mV s^{-1}, (e) Nyquist plots of $MnMo_6$−$2NH_2$−GO-2, $MnMo_6$−$2NH_2$, and $MnMo_6$/GO, and (f) cycling performance $MnMo_6$−$2NH_2$−GO-2 at a current density of 1000 mA g^{-1}.

and Figure S4 of the Supporting Information). To further detect the inner morphology, TEM has been conducted, and it can be seen that $MnMo_6$−$2NH_2$ nanoparticles with ∼3 nm in diameter are uniformly distributed in the GO nanosheet (Figure 2d). In addition, an element mapping image shows that Mn, Mo, N, and O are uniformly distributed in the nanosheet (Figure 2f). Besides, atomic force microscopy (AFM) tests have been conducted to evaluate the thickness of the samples, and $MnMo_6$−$2NH_2$−GO-2 shows a thickness of ∼1.1 nm (panels a and b of Figure 3). To reveal the possible interaction between $MnMo_6$−$2NH_2$ and GO, $MnMo_6$ as the contrast sample without amino groups has been applied to replace $MnMo_6$−$2NH_2$ and prepared $MnMo_6$/GO following similar steps. However, the morphology of $MnMo_6$/GO shows that $MnMo_6$ in a larger size (50−200 nm) is non-uniformly distributed in GO, implying that the strong interaction generated between $MnMo_6$−$2NH_2$ and GO might ensure the uniform distribution and inhibit the self-aggregation of $MnMo_6$−$2NH_2$ (Figure S3 of the Supporting Information).

As a comparison, $MnMo_6$−$2NH_2$−GO-x (x = 1, 2, and 3) with changed $MnMo_6$−$2NH_2$ and an intact amount of GO in the precursor have been prepared. $MnMo_6$−$2NH_2$−GO-1 with a smaller amount of $MnMo_6$−$2NH_2$ displays uniform morphology in the TEM tests, while some aggregated $MnMo_6$−$2NH_2$ nanocubes have been envisioned in $MnMo_6$−$2NH_2$−GO-3 with larger loading of $MnMo_6$−$2NH_2$ when compared to $MnMo_6$−$2NH_2$−GO-2 (Figure S5 of the Supporting Information). In addition, $MnMo_6$−$2NH_2$−GO-x (x = 2, 4, and 5) with changed amounts of GO and an intact amount of $MnMo_6$−$2NH_2$ have also been prepared as another group of comparisons. For $MnMo_6$−$2NH_2$−GO-4, the lower content of GO results in obvious aggregation of $MnMo_6$−$2NH_2$ and ∼300 nm nanocubes can be observed (Figure S6 of the Supporting Information). In contrast, almost no aggregation of $MnMo_6$−$2NH_2$ can be detected in $MnMo_6$−

https://dx.doi.org/10.1021/acs.energyfuels.0c03482
Energy Fuels 2020, 34, 16968−16977

$2NH_2$−GO-5 with higher GO loading (Figure S6 of the Supporting Information). Therefore, a series of $MnMo_6$−$2NH_2$−GO-x (x = 1−5) with tunable morphology and compositions have been successfully prepared.

To reveal the interaction between $MnMo_6$−$2NH_2$ and GO, FTIR and Raman tests have been conducted. When $MnMo_6$−$2NH_2$−GO-2 is taken as an example for instance, the characteristic peaks observed at 1004, 1551, 1634, and 3130 cm^{-1} in the FTIR spectra correspond to the bonds of C−O, C═C, C═O, and C−H in GO, respectively. Besides, the new characteristic peaks at 934, 673, 1646, and 1564 cm^{-1} are ascribed to the tensile vibration of ν(Mo−O), ν(Mo−O−Mo), ν(C−N), and ν(N−H) of $MnMo_6$−$2NH_2$. The results indicate the integration of both $MnMo_6$−$2NH_2$ and GO in the hybrid materials (Figure 2b). To further prove it, the Raman spectra of $MnMo_6$−$2NH_2$, $MnMo_6$/GO, and $MnMo_6$−$2NH_2$−GO-2 have been tested and the peak/intensity ratios of D and G bands for GO in $MnMo_6$−$2NH_2$−GO-2 are obviously stronger than those of $MnMo_6$/GO (Figure S2 of the Supporting Information). This indicates that GO is partially reduced to RGO during the reaction, resulting in the decrease of surface oxygen groups and the enhancement of the D band (Figure S2 of the Supporting Information).[45] In addition, the peaks for $MnMo_6$−$2NH_2$ (i.e., 906 and 937 cm^{-1}) in $MnMo_6$−$2NH_2$−GO-2 are slightly shifted to 830 and 890 cm^{-1} when compared to those in $MnMo_6$−$2NH_2$ and $MnMo_6$/GO, respectively, indicating the strong interaction generated between $MnMo_6$−$2NH_2$ and GO.

To estimate the electronic state of the hybrid materials, X-ray photoelectron spectroscopy (XPS) tests have been conducted. The spectra demonstrate the existence of C, Mn, Mo, and O elements in $MnMo_6$−$2NH_2$−GO-2 (panels c−f of Figure 3). The C 1s spectrum shows that the binding energy peaks of 284.79, 285.79, 286.49, 287.19, and 288.89 eV are detected, which can be ascribed to C−C/C═C, C−N, C−O, C═O, and −COO bonds, respectively (Figure 3f). The existence of the C−N bond indicates that $MnMo_6$−$2NH_2$ and GO in $MnMo_6$−$2NH_2$−GO-2 electrode materials are possibly connected by a covalent bond. There are two peaks of 232.5 and 235.85 eV in the energy spectrum of Mo 3d, corresponding to the binding energies of Mo $3d_{3/2}$ and Mo $3d_{5/2}$ in $MnMo_6$−$2NH_2$, respectively, ascribing to Mo^{6+} (Figure 3d).[46−52] In the energy spectrum of Mn 2p, two peaks (i.e., 641.9 and 653.85 eV) attributed to Mn $2P_{3/2}$ are observed (Figure 3e). On the basis of the XPS results, Mn^{3+} and Mo^{6+} are detected in $MnMo_6$−$2NH_2$−GO-2, which can predict that there are numerous changeable valences in $MnMo_6$−NH_2 (panels d and e of Figure 3).

Nitrogen (N_2) sorption tests have been applied to evaluate the porosity of the hybrid materials (Figure S8 of the Supporting Information). $MnMo_6$−$2NH_2$−GO-2 shows a specific surface area (S_{BET}) of 101 m^2 g^{-1} and a pore volume (V_t) of 0.88 cm^3 g^{-1}, while lower values are detected for $MnMo_6$/GO (S_{BET}, 68 m^2 g^{-1}; V_t, 0.30 cm^3 g^{-1}) and $MnMo_6$−$2NH_2$ (S_{BET}, 85 m^2 g^{-1}; V_t, 0.14 cm^3 g^{-1}), indicating that $MnMo_6$−$2NH_2$ and GO might have a synergistic effect on the improvement of the porosity (Figure S8 of the Supporting Information). The developed porosity of the hybrid materials might promote the rapid transfer of Li^+ and electrons and facilitate the full contact with the electrolyte, which would be expected to improve the battery performance.

Above all, a series of porous hybrid materials with tunable morphology and compositions have been successfully prepared, holding much promise as electrode materials in LIBs. The electrochemical performance of the hybrid materials was evaluated by assembling them into coin cells with lithium as the counter electrode and cycled between 3.0 and 0.01 V versus Li^+/Li. When $MnMo_6$−$2NH_2$−GO-2-based LIBs are taken as an example for instance, they present a small envelope peak at about 0.7 V, which can be distinguished from the CV curve in the first cycle (Figure 4d). The signal indicates the formation of a solid electrolyte interface (SEI) film in the first cycle, and the peak disappears in the subsequent cycle.[54] The SEI is a protecting layer formed on the complex electrode of LIBs as a result of electrolyte decomposition, mainly during the first cycle. In the first CV curve, there are two significant cathode peaks (i.e., ∼0.36 and ∼1.38 V) and anode peaks (i.e., ∼0.10 and ∼1.47 V), attributed to the reduction and oxidation of Mo in $MnMo_6$−$2NH_2$, respectively (Figure 4d).[53] The electrode materials of $MnMo_6$−$2NH_2$−GO-2 discharged to 0.01 V are also characterized by XPS tests (Figure S7 of the Supporting Information). The results show that, in addition to two peaks belonging to Mo^{6+}, there is a new peak that appeared at 231.7 eV, corresponding to the redox peak of Mo^{4+} in the CV curve (Figure 4d).[36] Therefore, there are mixed valences of Mo in the hybrid materials, proven to be electron sponges with high redox properties and are capable of electron donating and withdrawing. Additionally, it is observed that the binding energy positions of 642.3 and 655.1 eV are ascribed to two peaks of Mn $2p_{3/2}$ and Mn $2p_{3/2}$ in the energy spectrum of Mn 2p, respectively, implying the remaining trivalent form of Mn when discharged to 0.01 V (Figure S7 of the Supporting Information). This result suggests that $MnMo_6$−$2NH_2$ in the hybrid material can be easily triggered and possesses redox properties during battery tests.

Besides, the CV curve of $MnMo_6$−$2NH_2$−GO-2 is almost overlapped after the first cycle, showing excellent cycle stability when applied as anode materials in LIBs. When the current density is 100 mA g^{-1}, the charge−discharge curves of the 1st, 5th, 10th, and 50th cycles of the $MnMo_6$−$2NH_2$−GO-2 hybrid material are shown in Figure 4c. The discharge capacity of $MnMo_6$−$2NH_2$−GO-2-based LIBs in the first cycle is 1642 mAh g^{-1}, which decreases to 1077 mAh g^{-1} in the second cycle. This might be due to the formation of the SEI film that leads to the significant decrease of capacity in the initial few cycles, commonly existing in the LIB electrode. In addition, the cycling stabilities of $MnMo_6$−$2NH_2$, $MnMo_6$/GO, and $MnMo_6$−$2NH_2$−GO-2 at a current density of 100 mA g^{-1} have been tested (Figure 4a). The first cycle discharge capacity of $MnMo_6$−$2NH_2$−GO-2 is 1642 mAh g^{-1} and maintains up to 1143 mAh g^{-1} after 100 cycles with a capacity retention rate of 69.6% (Figure 4a). In contrast, $MnMo_6$−$2NH_2$ and $MnMo_6$/GO display relatively lower discharge capacity in the first cycle ($MnMo_6$−$2NH_2$, 1367 mAh g^{-1}; $MnMo_6$/GO, 1200 mAh g^{-1}) yet largely decrease after 100 cycles ($MnMo_6$−$2NH_2$, 125 mAh g^{-1}; $MnMo_6$/GO, 517 mAh g^{-1}) with capacity retentions of only 9 and 43%, respectively. The results reveal the superiority of $MnMo_6$−$2NH_2$−GO-2 over $MnMo_6$−$2NH_2$ and $MnMo_6$/GO, suggesting the synergistic effect of $MnMo_6$−$2NH_2$ and GO in the improvement of battery performance. To prove the vital role of $MnMo_6$−$2NH_2$ in LIBs, we applied ethylenediamine (EDA) and p-phenylenediamine (PDA) that could react with GO and be treated under similar processes to synthesize the contrast samples. The results show that the EDA−GO-2-based battery has no capacity, and the capacity of the PDA−GO-2-based battery

https://dx.doi.org/10.1021/acs.energyfuels.0c03482
Energy Fuels 2020, 34, 16968−16977

is only 1193 mAh g^{-1} in the first cycle at 100 mA g^{-1} and quickly decreases to 669 mAh g^{-1} in the second cycle (Figure S11 of the Supporting Information). The much poorer performance of contrast samples can be ascribed to the lack of a core component, such as $MnMo_6$−$2NH_2$, with a high redox ability that has a giant influence on the performance of LIBs. Besides, the reversible capacity of $MnMo_6$−$2NH_2$−GO-2 is about 1143 mAh g^{-1} at 100 mA g^{-1}, whereas the theoretical capacity of $MnMo_6$−$2NH_2$−GO-2 is calculated to be about 339.5 mAh g^{-1} (for details, see the Supporting Information). We speculate that this value exceeding the theoretical value is possibly attributed to the hybrid behavior of the battery supercapacitor on account of $MnMo_6$−$2NH_2$−GO-2.[49,50] The battery component is caused by the reversible redox reactions of Mo during the lithiation/delithiation cycles. At the same time, the capacitive behavior that is ascribed to GO also promotes the performance.

EIS of $MnMo_6$−$2NH_2$−GO-2, $MnMo_6$−$2NH_2$, and $MnMo_6$/GO has also been conducted to reveal the transmission of these samples (Figure 4e). $MnMo_6$−$2NH_2$−GO-2 displays a much smaller charge transfer resistance (∼210.2 Ω) compared to $MnMo_6$−$2NH_2$ (∼800.7 Ω) and $MnMo_6$/GO (∼386.1 Ω). The Nyquist curve shows that the semicircle diameters of the $MnMo_6$−$2NH_2$−GO-2 electrode material in the high-frequency regions are smaller after three charge/discharge cycles in comparison to $MnMo_6$/GO and $MnMo_6$−$2NH_2$, indicating the lower contact resistance and charge transfer resistance of $MnMo_6$−$2NH_2$−GO-2 (Figure 4e). This demonstrates the faster charge transfer kinetic for $MnMo_6$−$2NH_2$−GO-2, which is more favorable for LIBs. The ability of lithiation/delithiation is also the key factor to judge whether the LIB electrode material can be used in practice. For this reason, we have tested the rate capacity performance of $MnMo_6$−$2NH_2$−GO-2 as anode materials in the voltage range from 0.01 to 3.0 V and current density range from 0.1 to 5 A g^{-1} (Figure 4b). It can be seen from the rate performance that the first discharge capacity at 0.1 A g^{-1} is tested to be 1641 mAh g^{-1} for $MnMo_6$−$2NH_2$−GO-2, gradually decays in the next cycle, and is finally maintained at 1143 mAh g^{-1}. It can also be reversibly cycled at various current densities; the average specific capacities are approximately 966, 851, 739, 574, 455, and 301 mAh g^{-1} at the current densities of 0.2, 0.5, 1, 2, 3, and 5 A g^{-1}, respectively. Besides, when the current density is reduced back to 0.1 A g^{-1} after 70 cycles, a high capacity of 1040 mAh g^{-1} is immediately resumed, suggesting the good reversibility of the $MnMo_6$−$2NH_2$−GO-2 electrode (Figure 4b). In contrast, $MnMo_6$/GO can only be restored to 780 mAh g^{-1} when the current density returns to 0.1 A g^{-1} after 70 cycles. The rate performance of $MnMo_6$−$2NH_2$−GO-2 is much better than that of $MnMo_6$/GO, implying that the covalent interaction between $MnMo_6$−$2NH_2$ and GO indeed has a positive effect on the improvement of the battery performance (Figure 4b). In addition, $MnMo_6$−$2NH_2$−GO-2 exhibits extraordinary long-term cycling performance, and reversible capacities of 643 and 555 mAh g^{-1} can be achieved after 200 and 500 cycles at 1 A g^{-1}, respectively (Figure 4f). From the above-mentioned experimental data, we can envision that the battery property of $MnMo_6$−$2NH_2$−GO-2 is better than both the single component and contrast samples without covalent interactions. This might be ascribed to the strong effect of the covalent chemical bond existing between $MnMo_6$−$2NH_2$ and GO that can inhibit the dissolution of POMs in an electrolyte and enhance the overall transmission and electrochemical activity to boost the battery performance.

After that, we have further studied the effects of different GO ($MnMo_6$−$2NH_2$−GO-1 and $MnMo_6$−$2NH_2$−GO-3) and $MnMo_6$−$2NH_2$ contents ($MnMo_6$−$2NH_2$−GO-4 and $MnMo_6$−$2NH_2$−GO-5) on the electrochemical properties (Figures S9 and S10 of the Supporting Information). $MnMo_6$−$2NH_2$−GO-1 and $MnMo_6$−$2NH_2$−GO-3 show lower capacity and poorer cycle performance and rate capability than $MnMo_6$−$2NH_2$−GO-2. For $MnMo_6$−$2NH_2$−GO-1, the poorer performance might be attributed to the lower GO loading in $MnMo_6$−$2NH_2$−GO-1, resulting in relatively poorer conductivity (Figure S9 of the Supporting Information). On the contrary, the higher concentration of GO loading in $MnMo_6$−$2NH_2$−GO-3 will increase the folding degree of GO, which will further affect the distribution of $MnMo_6$−$2NH_2$ to hinder the contact between Li^+ or electrons and active substances during battery cycles. For $MnMo_6$−$2NH_2$−GO-4 and $MnMo_6$−$2NH_2$−GO-5, less content of $MnMo_6$−$2NH_2$ in $MnMo_6$−$2NH_2$−GO-5 will lead to the insufficient amount of active components (Figure S10 of the Supporting Information). However, the excessive addition of $MnMo_6$−$2NH_2$ in $MnMo_6$−$2NH_2$−GO-4 will lead to the agglomeration of $MnMo_6$−$2NH_2$ in the material compared to $MnMo_6$−$2NH_2$−GO-4 and result in reducing the battery performance (Figure S10 of the Supporting Information).

As mentioned above, we have synthesized a series of powerful anode materials for LIBs. The covalent bonding generated between $MnMo_6$−$2NH_2$ and GO has largely improved the chemical stability and transmission of the hybrid materials, which is also beneficial for the multi-electron transfer process in LIBs. The advantages of $MnMo_6$−$2NH_2$−GO-x can be summarized as follows: (1) It was confirmed by various characterizations that these hybrid materials have a covalent bond, which can promote the uniform dispersion of $MnMo_6$−$2NH_2$ and act as the electron bridge to facilitate the transmission of electrons and Li^+. (2) The epoxy functional groups on the surface of GO have partially reacted with amino groups of $MnMo_6$−$2NH_2$, and GO is simultaneously reduced to RGO with improved conductivity. (3) The covalent bond acting as an electronic bridge can ensure the close contact between GO and $MnMo_6$−$2NH_2$ to construct a conductive system, which would sufficiently integrate an electron sponge with a conductive substrate together. (4) The strong covalent connection between GO and $MnMo_6$−$2NH_2$ can effectively inhibit the dissolution of $MnMo_6$−$2NH_2$ in the electrolyte and improve the cycle stability of the battery.

4. CONCLUSION

In summary, we have successfully prepared a series of $MnMo_6$−$2NH_2$−GO ultrathin nanosheets (as thin as ∼1.1 nm) through the self-assembly of $MnMo_6$−$2NH_2$ and GO. The synergistic integration of $MnMo_6$−$2NH_2$ and GO in the ultrathin nanosheets can serve the role of gathering POMs and a conductive substrate in a system to overcome the problems of solubility and poor conductivity of POMs. Thus, obtained materials can combine both the advantages of $MnMo_6$−$2NH_2$ and GO, in which $MnMo_6$−$2NH_2$ serving as the electron sponge can be covalently connected with GO and applied as high-efficiency anode materials for LIBs. Notably, $MnMo_6$−$2NH_2$−GO-2 exhibits a reversible capacity of 1143 mAh g^{-1} (0.1 A g^{-1}) after 100 cycles, and the capacity retention is nearly 100% at 1000 mA g^{-1} over 500 cycles, the highest

https://dx.doi.org/10.1021/acs.energyfuels.0c03482
Energy Fuels 2020, 34, 16968−16977

among POM-based electrode materials. In addition, it also shows excellent rate capability (301 mAh g^{-1} in 5 A g^{-1}). This study not only provides a promising pathway to efficiently connect POMs with conductive materials at the molecular level but also proposes a new strategy to develop novel electrode materials for LIBs.

■ ASSOCIATED CONTENT

Supporting Information

The Supporting Information is available free of charge at https://pubs.acs.org/doi/10.1021/acs.energyfuels.0c03482.

Experimental details and additional characterizations (PDF)

■ AUTHOR INFORMATION

Corresponding Authors

Yifa Chen − *Jiangsu Key Laboratory of Biofunctional Materials, School of Chemistry and Materials Science, Nanjing Normal University, Nanjing, Jiangsu 210023, People's Republic of China; School of Chemistry, South China Normal University, Guangzhou, Guangdong 510006, People's Republic of China;* orcid.org/0000-0002-1718-6871; Email: chyf927821@163.com

Ya-Qian Lan − *Jiangsu Key Laboratory of Biofunctional Materials, School of Chemistry and Materials Science, Nanjing Normal University, Nanjing, Jiangsu 210023, People's Republic of China; School of Chemistry, South China Normal University, Guangzhou, Guangdong 510006, People's Republic of China;* orcid.org/0000-0002-2140-7980; Email: yqlan@njnu.edu.cn

Authors

Jia-Nan Chang − *Jiangsu Key Laboratory of Biofunctional Materials, School of Chemistry and Materials Science, Nanjing Normal University, Nanjing, Jiangsu 210023, People's Republic of China*

Mi Zhang − *School of Chemistry, South China Normal University, Guangzhou, Guangdong 510006, People's Republic of China*

Guang-Kuo Gao − *Jiangsu Key Laboratory of Biofunctional Materials, School of Chemistry and Materials Science, Nanjing Normal University, Nanjing, Jiangsu 210023, People's Republic of China; School of Materials Science and Engineering, College of Chemical and Environmental Engineering, Harbin University of Science and Technology, Harbin, Heilongjiang 150040, People's Republic of China*

Meng Lu − *Jiangsu Key Laboratory of Biofunctional Materials, School of Chemistry and Materials Science, Nanjing Normal University, Nanjing, Jiangsu 210023, People's Republic of China*

Yi-Rong Wang − *Jiangsu Key Laboratory of Biofunctional Materials, School of Chemistry and Materials Science, Nanjing Normal University, Nanjing, Jiangsu 210023, People's Republic of China*

Cheng Jiang − *Jiangsu Key Laboratory of Biofunctional Materials, School of Chemistry and Materials Science, Nanjing Normal University, Nanjing, Jiangsu 210023, People's Republic of China*

Shun-Li Li − *Jiangsu Key Laboratory of Biofunctional Materials, School of Chemistry and Materials Science, Nanjing Normal University, Nanjing, Jiangsu 210023, People's Republic of China*

Complete contact information is available at: https://pubs.acs.org/10.1021/acs.energyfuels.0c03482

Author Contributions

†Jia-Nan Chang, Mi Zhang, and Guang-Kuo Gao contributed equally to this work.

Notes

The authors declare no competing financial interest.

■ ACKNOWLEDGMENTS

This work was financially supported by the National Natural Science Foundation of China (NSFC, 21871141, 21871142, 21701085, and 21901122), the Natural Science Foundation (NSF) of Jiangsu Province of China (BK20171032), the Natural Science Research of Jiangsu Higher Education Institutions of China (17KJB150025 and 19KJB150011), a project funded by the China Postdoctoral Science Foundation (2018M630572 and 2019M651873), the Priority Academic Program Development of Jiangsu Higher Education Institutions, and the Foundation of Jiangsu Collaborative Innovation Center of Biomedical Functional Materials.

■ REFERENCES

(1) Chu, S.; Majumdar, A. Opportunities and challenges for a sustainable energy future. *Nature* **2012**, *488*, 294−303.

(2) Fukuzumi, S. Production of liquid solar fuels and their use in fuel cells. *Joule* **2017**, *1*, 689−738.

(3) Chan, C. K.; Peng, H.; Liu, G.; McIlwrath, K.; Zhang, X. F.; Huggins, R. A.; Cui, Y. High-performance lithium battery anodes using silicon nanowires. *Nat. Nanotechnol.* **2008**, *3*, 31−35.

(4) Yu, K.; Pan, X.; Zhang, G.; Liao, X.; Zhou, X.; Yan, M.; Xu, L.; Mai, L. Nanowires in energy storage devices: Structures, synthesis, and applications. *Adv. Energy Mater.* **2018**, *8*, 1802369.

(5) Wei, Q.; Xiong, F.; Tan, S.; Huang, L.; Lan, E. H.; Dunn, B.; Mai, L. Porous one-dimensional nanomaterials: Design, fabrication and applications in electrochemical energy torage. *Adv. Mater.* **2017**, *29*, 1602300.

(6) Zhou, G.; Xu, L.; Hu, G.; Mai, L.; Cui, Y. Nanowires for electrochemical energy storage. *Chem. Rev.* **2019**, *119*, 11042−11109.

(7) Manthiram, A. A reflection on lithium-ion battery cathode chemistry. *Nat. Commun.* **2020**, *11*, 1550.

(8) Qiao, L.; Judez, X.; Rojo, T.; Armand, M.; Zhang, H. Review-polymer electrolytes for sodium batteries. *J. Electrochem. Soc.* **2020**, *167*, 070534.

(9) Winter, M.; Barnett, B.; Xu, K. Before Li ion batteries. *Chem. Rev.* **2018**, *118*, 11433−11456.

(10) Lin, D.; Liu, Y.; Cui, Y. Reviving the lithium metal anode for high-energy batteries. *Nat. Nanotechnol.* **2017**, *12*, 194−206.

(11) Wu, H.; Chan, G.; Choi, J. W.; Ryu, I.; Yao, Y.; McDowell, M. T.; Lee, S. W.; Jackson, A.; Yang, Y.; Hu, L.; Cui, Y. Stable cycling of double-walled silicon nanotube battery anodes through solid-electrolyte interphase control. *Nat. Nanotechnol.* **2012**, *7*, 310−315.

(12) Xie, J.; Lu, Y.-C. A retrospective on lithium-ion batteries. *Nat. Commun.* **2020**, *11*, 2499.

(13) He, S.; Zeng, J.; Habte, B. T.; Jiang, F. Numerical reconstruction of microstructure of graphite anode of lithium-ion battery. *Sci. Bull.* **2016**, *61*, 656−664.

(14) Marcoux, P. R.; Hasenknopf, B.; Vaissermann, J.; Gouzerh, P. Developing remote metal binding sites in heteropolymolybdates. *Eur. J. Inorg. Chem.* **2003**, *2003*, 2406−2412.

(15) Peng, C.; Mercer, M. P.; Skylaris, C.-K.; Kramer, D. Lithium intercalation edge effects and doping implications for graphite anodes. *J. Mater. Chem. A* **2020**, *8*, 7947−7955.

(16) Cheng, X.-B.; Zhao, M.-Q.; Chen, C.; Pentecost, A.; Maleski, K.; Mathis, T.; Zhang, X.-Q.; Zhang, Q.; Jiang, J.; Gogotsi, Y.

Nanodiamonds suppress the growth of lithium dendrites. *Nat. Commun.* **2017**, *8*, 336.
(17) Jana, A.; Woo, S. I.; Vikrant, K. S. N.; García, R. E. Electrochemomechanics of lithium dendrite growth. *Energy Environ. Sci.* **2019**, *12*, 3595−3607.
(18) Ke, X.; Wang, Y.; Dai, L.; Yuan, C. Cell failures of all-solid-state lithium metal batteries with inorganic solid electrolytes: Lithium dendrites. *Energy Storage Mater.* **2020**, *33*, 309−328.
(19) Walsh, J. J.; Bond, A. M.; Forster, R. J.; Keyes, T. E. Hybrid polyoxometalate materials for photo(electro-) chemical applications. *Coord. Chem. Rev.* **2016**, *306*, 217−234.
(20) Weinstock, I. A.; Schreiber, R. E.; Neumann, R. Dioxygen in polyoxometalate mediated reactions. *Chem. Rev.* **2018**, *118*, 2680−2717.
(21) Proust, A.; Matt, B.; Villanneau, R.; Guillemot, G.; Gouzerh, P.; Izzet, G. Functionalization and post-functionalization: A step towards polyoxometalate-based materials. *Chem. Soc. Rev.* **2012**, *41*, 7605−7622.
(22) Zhang, Z.-M.; Zhang, T.; Wang, C.; Lin, Z.; Long, L.-S.; Lin, W. Photosensitizing metal-organic framework enabling visible-light-driven proton reduction by a Wells-Dawson-type polyoxometalate. *J. Am. Chem. Soc.* **2015**, *137*, 3197−3200.
(23) Li, N.; Liu, J.; Dong, B.-X.; Lan, Y.-Q. Polyoxometalate-based compounds for photo and electrocatalytic applications. *Angew. Chem., Int. Ed.* **2020**, DOI: 10.1002/anie.202008054.
(24) Li, N.; Liu, J.; Liu, J.-J.; Dong, L.-Z.; Li, S.-L.; Dong, B.-X.; Kan, Y.-H.; Lan, Y.-Q. Self-assembly of a phosphate-centered polyoxotitanium cluster: Discovery of the heteroatom Keggin family. *Angew. Chem., Int. Ed.* **2019**, *58*, 17260−17264.
(25) Zhang, Y.; Liu, J.; Li, S.-L.; Su, Z.-M.; Lan, Y.-Q. Polyoxometalate-based materials for sustainable and clean energy conversion and storage. *Energy Chem.* **2019**, *1*, 100021.
(26) Wang, Y.-R.; Huang, Q.; He, C.-T.; Chen, Y.; Liu, J.; Shen, F.-C.; Lan, Y.-Q. Oriented electron transmission in polyoxometalate-metalloporphyrin organic framework for highly selective electroreduction of CO_2. *Nat. Commun.* **2018**, *9*, 4466.
(27) Chen, J.-J.; Symes, M. D.; Cronin, L. Highly reduced and protonated aqueous solutions of $[P_2W_{18}O_{62}]^{6-}$ for on-demand hydrogen generation and energy storage. *Nat. Chem.* **2018**, *10*, 1042−1047.
(28) Chen, J.-J.; Ye, J.-C.; Zhang, X.-G.; Symes, M. D.; Fan, S.-C.; Long, D.-L.; Zheng, M.-S.; Wu, D.-Y.; Cronin, L.; Dong, Q.-F. Design and performance of rechargeable sodium ion batteries, and symmetrical Li-ion batteries with supercapacitor-like power density based upon polyoxovanadates. *Adv. Energy Mater.* **2018**, *8*, 1701021.
(29) Ju, L.; Wang, G.; Liang, K.; Wang, M.; Sterbinsky, G. E.; Feng, Z.; Yang, Y. Significantly improved cyclability of conversion-type transition metal oxyfluoride cathodes by homologous passivation layer reconstruction. *Adv. Energy Mater.* **2020**, *10*, 1903333.
(30) Chen, J.-J.; Symes, M. D.; Fan, S.-C.; Zheng, M.-S.; Miras, H. N.; Dong, Q.-F.; Cronin, L. High-performance polyoxometalate-based cathode materials for rechargeable lithium-ion batteries. *Adv. Mater.* **2015**, *27*, 4649−4654.
(31) Wang, H.; Hamanaka, S.; Nishimoto, Y.; Irle, S.; Yokoyama, T.; Yoshikawa, H.; Awaga, K. In perando x-ray absorption fine structure studies of polyoxometalate molecular cluster batteries: Polyoxometalates as electron sponges. *J. Am. Chem. Soc.* **2012**, *134*, 4918−4924.
(32) Huang, Q.; Wei, T.; Zhang, M.; Dong, L.-Z.; Zhang, A. M.; Li, S.-L.; Liu, W.-J.; Liu, J.; Lan, Y.-Q. A highly stable polyoxometalate-based metal-organic framework with π-π stacking for enhancing lithium ion battery performance. *J. Mater. Chem. A* **2017**, *5*, 8477−8483.
(33) Wei, T.; Zhang, M.; Wu, P.; Tang, Y.-J.; Li, S.-L.; Shen, F.-C.; Wang, X.-L.; Zhou, X.-P.; Lan, Y.-Q. POM-based metal-organic framework/reduced graphene oxide nanocomposites with hybrid behavior of battery-supercapacitor for superior lithium storage. *Nano Energy* **2017**, *34*, 205−214.
(34) Yue, Y.; Li, Y.; Bi, Z.; Veith, G. M.; Bridges, C. A.; Guo, B.; Chen, J.; Mullins, D. R.; Surwade, S. P.; Mahurin, S. M.; Liu, H.; Paranthaman, M. P.; Dai, S. A POM-organic framework anode for Li-ion battery. *J. Mater. Chem. A* **2015**, *3*, 22989−22995.
(35) Paek, S.-M.; Yoo, E.; Honma, I. Enhanced cyclic performance and lithium storage capacity of SnO_2/graphene nanoporous electrodes with three-dimensionally delaminated flexible structure. *Nano Lett.* **2009**, *9*, 72−75.
(36) Zhou, D.; Han, B.-H. Graphene-based nanoporous materials assembled by mediation of polyoxometalate nanoparticles. *Adv. Funct. Mater.* **2010**, *20*, 2717−2722.
(37) Kawasaki, N.; Wang, H.; Nakanishi, R.; Hamanaka, S.; Kitaura, R.; Shinohara, H.; Yokoyama, T.; Yoshikawa, H.; Awaga, K. Nanohybridization of polyoxometalate clusters and single-wall carbon nanotubes: Applications in molecular cluster batteries. *Angew. Chem., Int. Ed.* **2011**, *50*, 3471−3474.
(38) Giusti, A.; Charron, G.; Mazerat, S.; Compain, J.-D.; Mialane, P.; Dolbecq, A.; Rivière, E.; Wernsdorfer, W.; Ngo Biboum, R.; Keita, B.; Nadjo, L.; Filoramo, A.; Bourgoin, J.-P.; Mallah, T. Magnetic bistability of individual single-molecule magnets grafted on single-wall carbon nanotubes. *Angew. Chem., Int. Ed.* **2009**, *48*, 4949−4952.
(39) Xie, J.; Zhang, Y.; Han, Y.; Li, C. High-capacity molecular scale conversion anode enabled by hybridizing cluster-type framework of high loading with amino-functionalized graphene. *ACS Nano* **2016**, *10*, 5304−5313.
(40) Liang, M.; Zhi, L. Graphene-based electrode materials for rechargeable lithium batteries. *J. Mater. Chem.* **2009**, *19*, 5871−5878.
(41) Ji, Y.; Huang, L.; Hu, J.; Streb, C.; Song, Y.-F. Polyoxometalate-functionalized nanocarbon materials for energy conversion, energy storage and sensor systems. *Energy Environ. Sci.* **2015**, *8*, 776−789.
(42) Huang, L.; Hu, J.; Ji, Y.; Streb, C.; Song, Y.-F. Pyrene-Anderson-modified CNTs as anode materials for lithium-ion batteries. *Chem. - Eur. J.* **2015**, *21*, 18799−18804.
(43) Ma, D.; Liang, L.; Chen, W.; Liu, H.; Song, Y.-F. Covalently tethered polyoxometalate-pyrene hybrids for noncovalent sidewall functionalization of single-walled carbon nanotubes as high-performance anode material. *Adv. Funct. Mater.* **2013**, *23*, 6100−6105.
(44) Abouimrane, A.; Compton, O. C.; Amine, K.; Nguyen, S. T. Non-annealed graphene paper as a binder-free anode for lithium-ion batteries. *J. Phys. Chem. C* **2010**, *114*, 12800−12804.
(45) Saha, U.; Jaiswal, R.; Goswami, T. H. A facile bulk production of processable partially reduced graphene oxide as superior supercapacitor electrode material. *Electrochim. Acta* **2016**, *196*, 386−404.
(46) Wang, D.; Luan, C.; Zhang, W.; Liu, X.; Sun, L.; Liang, Q.; Qin, T.; Zhao, Z.; Zhou, Y.; Wang, P.; Zheng, W. Zipper-inspired SEI film for remarkably enhancing the stability of Li metal anode via nucleation barriers controlled weaving of lithium pits. *Adv. Energy Mater.* **2018**, *8*, 1800650.
(47) Liu, B.; Xu, W.; Yan, P.; Kim, S. T.; Engelhard, M. H.; Sun, X.; Mei, D.; Cho, J.; Wang, C.-M.; Zhang, J.-G. Stabilization of Li metal anode in DMSO-based electrolytes via optimization of salt-solvent coordination for Li-O_2 batteries. *Adv. Energy Mater.* **2017**, *7*, 1602605.
(48) Judez, X.; Zhang, H.; Li, C.; González-Marcos, J. A.; Zhou, Z.; Armand, M.; Rodriguez-Martinez, L. M. Lithium bis(fluorosulfonyl)-imide/poly(ethylene oxide) polymer electrolyte for all solid-state Li-S cell. *J. Phys. Chem. Lett.* **2017**, *8*, 1956−1960.
(49) Cheng, X.-B.; Zhang, R.; Zhao, C.-Z.; Wei, F.; Zhang, J.-G.; Zhang, Q. A review of solid electrolyte interphases on lithium metal anode. *Adv. Sci.* **2016**, *3*, 1500213.
(50) Tian, H.; Seh, Z. W.; Yan, K.; Fu, Z.; Tang, P.; Lu, Y.; Zhang, R.; Legut, D.; Cui, Y.; Zhang, Q. Theoretical investigation of 2D layered materials as protective films for lithium and sodium metal anodes. *Adv. Energy Mater.* **2017**, *7*, 1602528.
(51) Fan, L.; Lei, S.; Kheimeh Sari, H. M.; Zhong, L.; Kakimov, A.; Wang, J.; Chen, J.; Liu, D.; Huang, L.; Hu, J.; Lin, L.; Li, X. Controllable S-Vacancies of monolayered Mo−S nanocrystals for highly harvesting lithium storage. *Nano Energy* **2020**, *78*, 105235.
(52) Liu, X.; Wang, Y.; Yang, Y.; Lv, W.; Lian, G.; Golberg, D.; Wang, X.; Zhao, X.; Ding, Y. A MoS_2/Carbon hybrid anode for high-performance Li-ion batteries at low temperature. *Nano Energy* **2020**, *70*, 104550.

(53) Zhang, A. M.; Zhang, M.; Lan, D.; Wang, H.-N.; Tang, Y.-J.; Wang, X.-L.; Dong, L.-Z.; Zhang, L.; Li, S.-L.; Lan, Y.-Q. Polyoxometalate-based metal-organic framework on carbon cloth with a hot-pressing method for high-performance lithium-ion batteries. *Inorg. Chem.* **2018**, *57*, 11726−11731.
(54) Gao, R.-M.; Zheng, Z.-J.; Wang, P.-F.; Wang, C.-Y.; Ye, H.; Cao, F.-F. Recent advances and prospects of layered transition metal oxide cathodes for sodium-ion batteries. *Energy Storage Mater.* **2020**, *30*, 9−26.
(55) Tang, Y.-J.; Wang, Y.; Wang, X.-L.; Li, S.-L.; Huang, W.; Dong, L.-Z.; Liu, C.-H.; Li, Y.-F.; Lan, Y.-Q. Molybdenum disulfide/nitrogen-doped reduced graphene oxide nanocomposite with enlarged interlayer spacing for electrocatalytic hydrogen evolution. *Adv. Energy Mater.* **2016**, *6*, 1600116.

https://dx.doi.org/10.1021/acs.energyfuels.0c03482
Energy Fuels 2020, 34, 16968−16977